2D Waveguided Bessel Beam Generated Using Integrated Metasurface-Based Plasmonic Axicon

Yulong Fan, Benoit Cluzel, Marlène Petit, Xavier Le Roux, Anatole Lupu, Andre De Lustrac

2D Waveguided Bessel Beam Generated using Integrated Metasurface-based Plasmonic Axicon

Yulong Fan[†], *Benoît Cluzel*[‡], *Marlène Petit*[‡], *Xavier Le Roux*[†], *Anatole Lupu*[*,†], *Andre de Lustrac*[†]

[†] Centre de Nanosciences et de Nanotechnologies, CNRS, Univ. Paris-Sud, Université Paris-Saclay, C2N – 10 Boulevard Thomas Gobert – 91120 Palaiseau cedex, France

[‡] Laboratoire Interdisciplinaire Carnot de Bourgogne, UMR 6303 CNRS - Université de Bourgogne Franche-Comté, 21078 Dijon, France

ABSTRACT: Near-field imaging of the propagation of a diffraction-free Bessel-type beam in a guided wave configuration generated by means of a metasurface-based axicon lens integrated on a silicon waveguide is reported. The operation of the axicon lens with a footprint as small as $11\mu m^2$ is based on local engineering of the effective index of the silicon waveguide with plasmonic nanoresonators. This generic approach, which can be adapted to different types of planar lightwave circuit platforms, offers the possibility to design nano-engineered optical devices based on the use of plasmonic resonators to control light at the nanoscale.

KEYWORDS: Axicon, Bessel beams, optical metasurfaces, surface plasmon resonances, Silicon photonics

As it have been known for a while, the phenomenon of diffraction is at the origin of one of a worst impairments for applications dealing with propagation of light beams in 2D or 3D unbounded optical media.[1] The convolution of spatial wavevectors forming the optical beam progressively leads to its widening with propagation distance. To counteract this issue, one of the non-diffracting beam solutions initially introduced and demonstrated by Durnin in 1987[2,3] consists in using Bessel functions with the following scalar form in cylindrical coordinates:

$$E(\rho,\phi,z) = A_0 \exp(ik_z z) J_n(k_\rho \rho) \exp(\pm in\phi) \quad (1)$$

where A_0 is the amplitude of the light wave, J_n is a Bessel function of order n, k_z and k_ρ are the corresponding longitudinal and radial wavevectors satisfying $\sqrt{k_z^2 + k_\rho^2} = k = \frac{2\pi}{\lambda}$ (λ being the wavelength), and ρ, ϕ and z indicate the radial, azimuthal and longitudinal components respectively. Since then Besselian type profile optical beams have attracted intensive research interest in several related domains like self-reconstruction,[4] faster-than-light X-waves,[5-8] optical pulling forces,[9-10] and bring out plenty of applications such as optical acceleration,[11] particle guiding[12-14] and micromanipulation,[15-16] nonlinear optics,[17-19] imaging,[20-21] optical lithography and microfabrication.[22-23] It should be noted however that ideal Bessel beams are spatially unbounded and carry infinite energy. Therefore, in practice, they can only be approximated by a truncated Bessel beam within the propagation distance up to several orders of magnitude of the wavelength by means of superposition of multiple plane waves.[24-25]

Conventionally, the Bessel beams are produced by an objective paired with an annular aperture at the front focal plane, as originally used by Durnin,[2,3] or by using an axicon lens proposed by Herman and Wiggins.[26] As the first approach suffers from a low efficiency, most of the incident waves being blocked by the aperture, the axicon lens approach was used more widely.[4,7-8,11-13,15-16,18-20,23,25-26] The advent of metasurface flat optics[27,28] offering advanced control of phase and amplitude on a subwavelength scale,[29] as well as management of the dispersion properties,[30] gave a new impetus to the development of axicon lens. Bessel beam generators based on metasurface exploiting this approach have been proposed and demonstrated.[31-33]

Although most efforts devoted to the propagation on non-diffractive beams are focused on free space optical applications, guided-wave optics is also looking for solutions to insure propagation of long distance collimated beams.[34,35] The conventional approach relies on self-collimation properties that can be obtained using 2D photonic crystal (PhC) structures.[36,37,38] However, its application is essentially limited to the propagation of single lobe Gaussian beams. The implementation of Bessel type profile requires an adaptation of both the phase and amplitude of the wavefront at the subwavelength scale. Performing this task using a PhC approach based on the interference of waves propagating forward and backward in a slab waveguide with a periodically modulated dielectric index pattern is far from trivial, if not impossible.

On the other hand, effective control at subwavelength scale for the phase and amplitude of the propagating wave can be obtained by integrating plasmonic nanoresonators at the top of the dielectric waveguide.[39] The underlying mechanism is based on the evanescent coupling of the fraction of the light propagating in the waveguide to plasmonic nanoresonators. The additional delay caused by the trapping of light in the nanoresonator results in a local phase shift of the guided-wave. The modification of the local phase and amplitude can thus be controlled by

adjusting the parameters of this hybrid metasurface-dielectric waveguide, namely the force of the evanescent coupling in plasmonic nanoresonators, their surface density, resonance frequency and quality factor. Within the validity limit of the homogenization approach, when all characteristic dimensions are well below the wavelength and the Bragg resonant interactions can be neglected, effective medium parameters such as the local effective index of the waveguide can be introduced.[39] Based on this approach, we recently performed an experimental demonstration of low-loss graded index metalens,[40] and ultra-compact 1.3/1.6μm wavelength demultiplexer.[41]

The objective of this work is to further reveal the potential of this enabling technology by experimentally demonstrating the efficient generation of a 2D guided wave Bessel-type beam obtained with a meta-axicon lens formed by a 2D array of plasmonic nanoresonators integrated on top of a silicon-on-insulator (SOI) waveguide, as shown in Fig. 1.

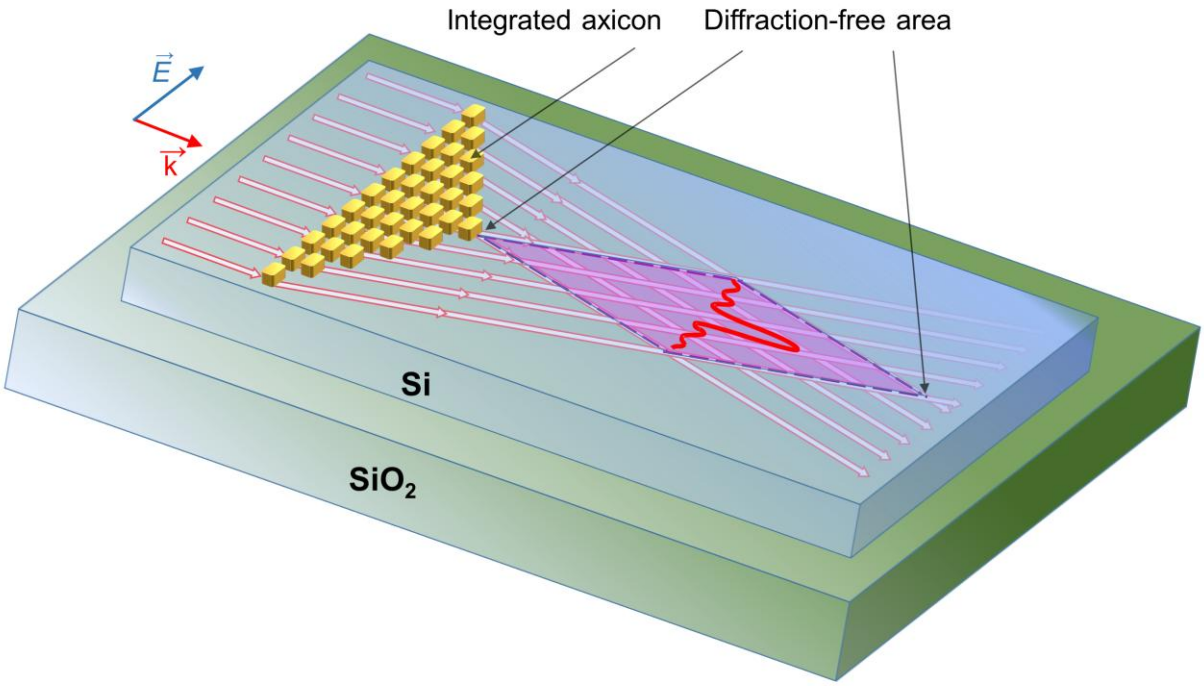

Figure 1. Schematic of Bessel beam generator formed by a 2D array of plasmonic nanoresonators integrated on an SOI waveguide.

DESIGN AND MODELING

The Bessel beam generator shown in Fig. 1 is formed of a D2 prismatic-shaped array (base length 8.02μm, height 2.85μm, i.e. a footprint of ~11μm^2) of gold plasmonic nanoresonators of dimensions 180nm×50nm×50nm. The spacing between adjacent cut-wires (CWs) nanoresonators in the direction transverse to the beam propagation d=100nm, while that along the beam propagation s=50nm. This choice of parameters for the resonant elements forming the meta-axicon is dictated by the need to conform to the homogeneisation approach. This is particularly critical when considering the periodicity p=100nm along the direction of light propagation,

which should be sufficiently small compared to the Bragg period (≈300nm) for the operating wavelength λ≈1550nm.

The 2D array of gold CWs is integrated at the top of SOI waveguide of a thickness of 220nm with a 5nm thick native silicon dioxide layer intentionally left to increase the resonance frequency of the CWs.[39] The operation of the meta-axicon is carried out in TE polarization, i.e. when guided-wave electric field is parallel to the base side of CWs array.

The effective index of the metasurface-dielectric hybrid waveguide corresponding to the meta-axicon area can readily be determined by numerical modeling with a subsequent retrieval procedure.[42,43] The parameters of Au, Si and SiO_2 used in the HFSS[44] numerical simulations are those provided by Palik.[45] To avoid CWs resonant absorption losses, we consider the operation of the meta-axicon in the spectral range from 1.5 to 1.64μm. At λ≈1.58μm that corresponds to the middle of meta-axicon working wavelength span, $n_{eff\ axicon}$≈3.0 whereas that of the bare silicon waveguide $n_{eff\ Si}$≈2.78. It is notably this difference in effective index $\Delta n = n_{eff\ axicon} - n_{eff\ Si}$≈0.22 which should provide ~3° of oblique angular refraction at the rear of the meta-axicon and the formation of the Bessel beam by effect of interference.

The predictions obtained on the basis of the effective medium approach are then verified by full 3D HFSS optical simulations of the meta-axicon. The calculated at λ=1.58μm wavelength distribution of light intensity propagating across the meta-axicon is illustrated in Fig. 2a. As can be seen the 10μm-wide incident Gaussian beam with the wave-vector k_{zi} is divided at the rear of the meta-axicon into two obliquely refracted beams. The corresponding wavefronts are underlined by white dashed lines and the outgoing wave-vectors k_{zo} are represented by white arrows. The two outgoing beams are matched in phase and interfere constructively after the

meta-axicon leading to an extended diffraction-free area. The angle of refraction between k_{zi} and k_{zo} estimated from Fig. 2a is about 4.2°. This angle of refraction is not far from that of 3.0° predicted in the effective medium approximation according to the Snell-Descartes law.

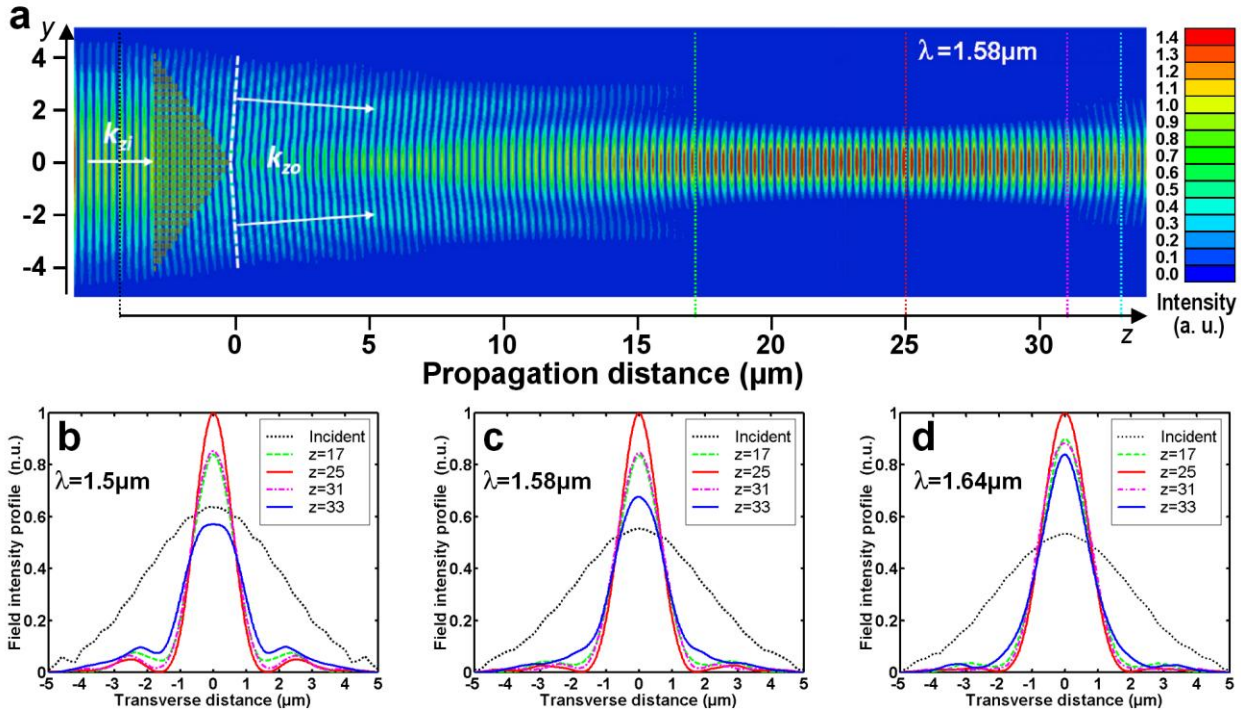

Figure 2. Top panel: a) HFSS modeling of light intensity propagating through the meta-axicon. Dotted colored lines indicate the position of cut-sections used to extract the beam intensity profile, and k_{zo} is the wave vector of the output beam. Bottom panel: Light intensity profile at different positions along the beam propagation direction z. Working wavelength: b) λ=1.5μm; c) λ=1.58μm; d) λ=1.64μm.

To highlight the transformation of the beam produced by the meta-axicon, the light intensity profiles at different wavelengths in the direction perpendicular to the direction of propagation z are displayed in the bottom panel of Fig. 2. As can be seen, the intensity of the waveguide mode before the meta-axicon is very close to the Gaussian profile. In contrast, the intensity profile of

the beam passed through the meta-axicon is very different. The first striking effect of propagation through the meta-axicon is the reduction of the main lobe spatial width by a factor of about two compared to that of the incident waveguide mode. The narrowest beam width is observed for z=25µm after the propagation distance of the meta-axicon. The narrowing of the spatial width of the main lobe is accompanied by the appearance of marked side lobes which are practically negligible when considering incident waveguide mode. This trend for the evolution of beam profile is valid for the entire meta-axicon operation wavelength span, although the extent of diffraction-free propagation is more pronounced for longer wavelength. According to the ratio between the integrated intensities of the profile of the output and input beam shown in Fig. 2d, the overall transmission of the axicon is evaluated at about 64%.

FABRICATION

The technological approach used to manufacture the meta-axicon is basically similar to that previously developed for the demonstration of metalens.[40] For the fabrication of the experimental meta-axicon sample, we used an undoped SOI wafer from SOITEC with a 220nm thick top silicon film separated from the Si substrate by a buried 2µm-thick SiO_2. The first step of NB4 electron-beam lithography using a PMMA positive resist is dedicated to the patterning of the CWs array and the alignment marks which are obtained through a deposition of 2nm film of Cr, then of a 50nm film of gold followed by a chemical lift-off process. The second NB4 electron-beam lithography using ZEP520A positive resist is devoted to the definition of the waveguide pattern. The resist remaining after development is used as soft mask for dry silicon etching by using an Inductive Coupled Plasma (ICP) method. Insets in Fig. 3 show scanning electron microscope (SEM) views of the fabricated device.

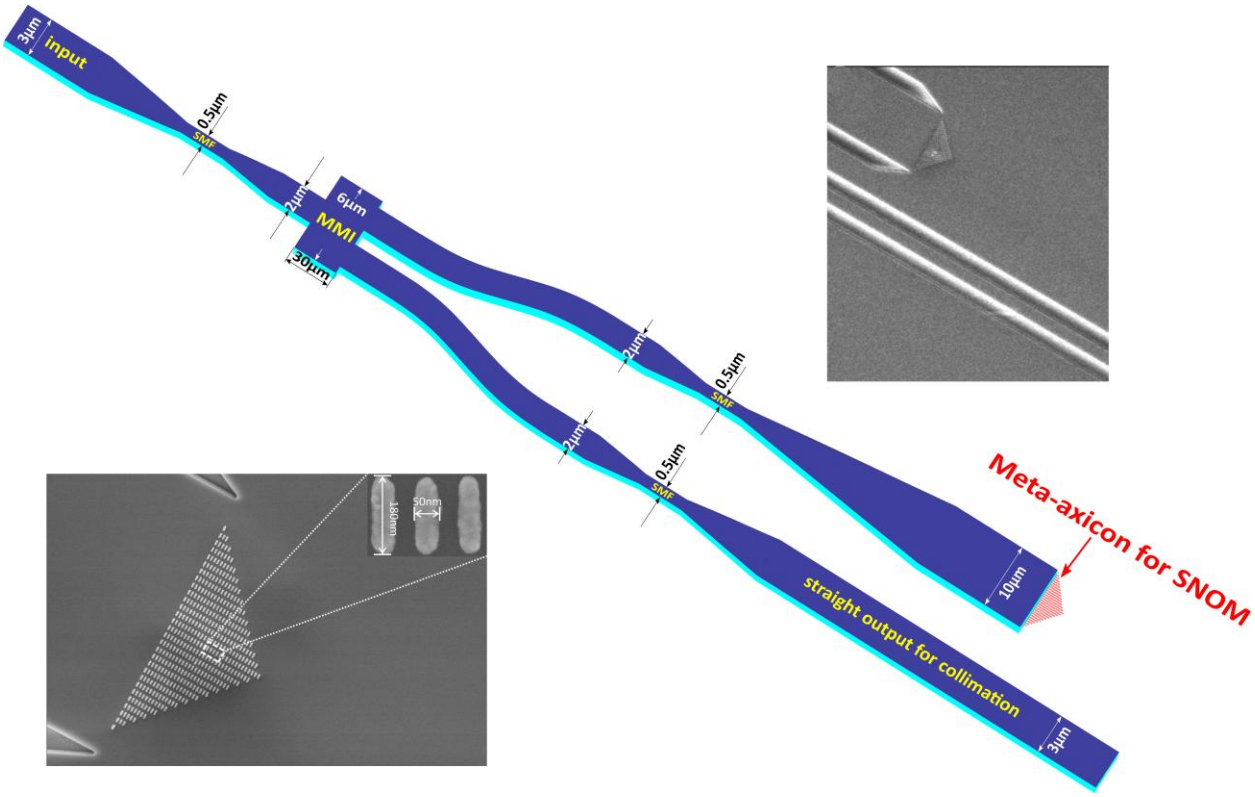

Figure 3. Sketch of the experimental sample with SOI input/output waveguides and the meta-axicon at the top of the SOI slab region. Insets show SEM image views of the fabricated device. Left: CWs based meta-axicon and enlarged view of the fabricated gold CWs; Right: Fragment of the input waveguide with meta-axicon and reference waveguide used for SNOM measurements optical alignment. The abbreviation SMF in the central panel denotes the single mode filter and MMI the multi-mode interference splitter.

MEASUREMENTS AND DISCUSSION

The scheme of the experimental sample, whose design has been specially adapted for near-field scanning optical (SNOM) measurements, is presented in the central panel of Fig. 3. The adaptation consists of using 1→2 multimode interference (MMI) splitter to separate the light

injected in the input waveguide into two arms: auxiliary and SNOM. The auxiliary arm is used to facilitate the alignment of the lensed fiber used for light injection with the input silicon waveguide. This is achieved by monitoring and maximizing the intensity of the transmitted light collected at the output of the auxiliary waveguide. The introduction of such a procedure is necessary because the SNOM arm terminating with the meta-axicon is not equipped with any waveguide for light collection. This is done intentionally to avoid as much as possible perturbing SNOM experiments with stray light caused by facets backreflection into the guided wave structure. It should also be noted that special care was given to the design of the SOI waveguides to insure light propagation only in the fundamental TE mode. This is achieved by using 200μm long tapered regions terminating with 0.5μm wide single-mode waveguide sections acting as higher order spatial mode filters (SMF in Fig. 3). This point was especially critical since SOI waveguides of a few microns in width are already intrinsically multimodes.

The experimental characterization based on an end-fire coupling and SNOM measurements in collection mode is shown in Fig. 4a. This experimental setup is detailed in the Methods section. It provides 2D maps of the electric field intensity distribution above the sample surface and the resulting image consists of a combination of the scattered field in the air and the evanescent decay of the guided modes on top of the silicon layer. The positions of the input waveguide and the axicon are displayed schematically with respect to the topography measured simultaneously with the optical images. The measurements shown in the paper are recorded for an input light having a TE polarization and a wavelength of 1.64μm for which the non-diffracting beam after the axicon is observed experimentally with the best contrast. Similar results, but with a lower signal to noise ratio, have also been obtained for other wavelengths between 1.5 and 1.64μm range. As illustrated by the SNOM measurements in Fig. 4a, the axicon transforms an incident

Gaussian beam into a Bessel-Gaussian beam. Figure 4b provides the SNOM measurement results for beam intensity profile before and after the axicon. The intensity of the input beam is fitted with a Gaussian profile while that of the output beam at z=25μm is fitted with a zero-order Bessel-Gaussian function. In both cases, a quantitative agreement is achieved and the overall behavior of the axicon is similar to that of the numerical forecasts.

For a more quantitative analysis of the Bessel-Gaussian beam outgoing from the axicon, we are then interested in near-field images recorded at the exit of the axicon only, but with a better discretization. We display in Fig. 4c the SNOM images obtained for two different distances between the sample surface and the probe. The “near-field” image is obtained at 4nm distance from the surface and the “far-field” image at 100nm. The sharp decrease in beam intensity exciting the axicon on the “far”-field image reveals the evanescent behavior of the collected waves whereas the remaining hot spots are related to the field scattered above the sample. The saturated bright spot on top of the axicon images corresponds to the radiation leakage of the axicon in free space.

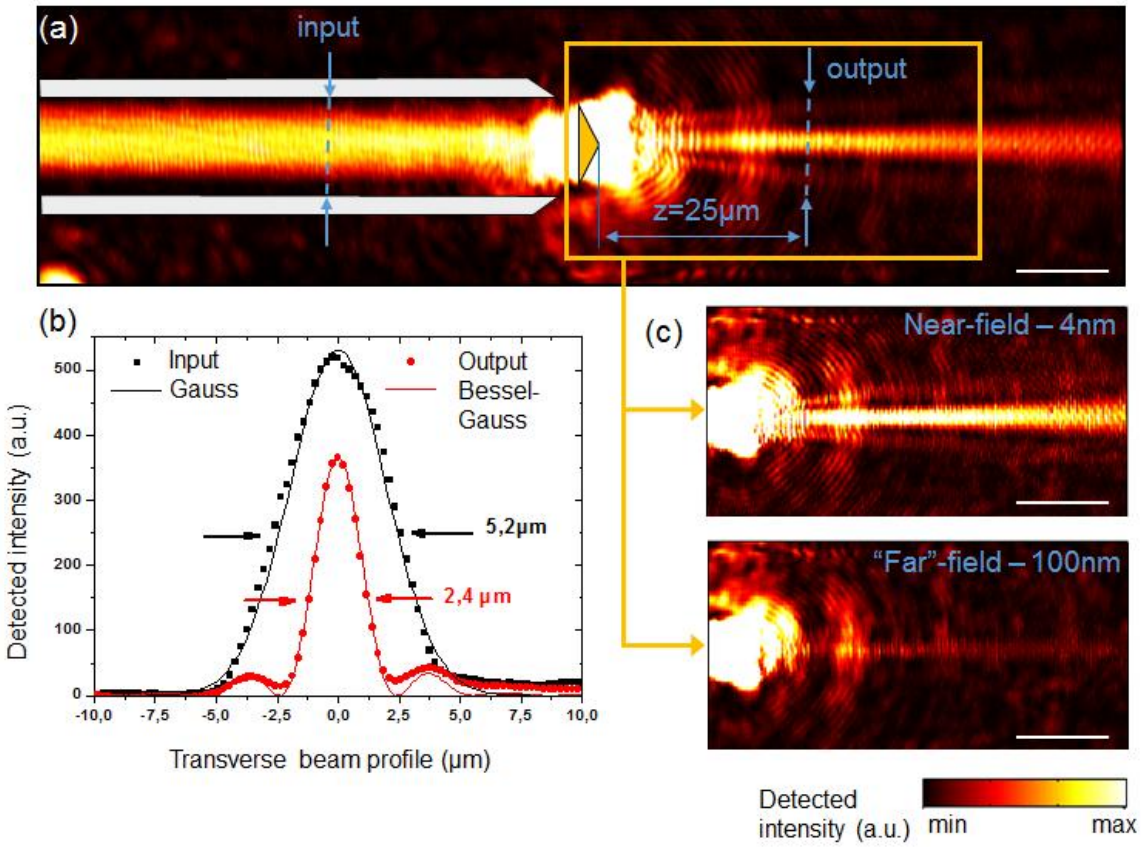

Figure 4. Scanning Near-field Optical Microscopy views of the axicon. Scale bar 10µm. a) general SNOM view of the axicon. The excitation waveguide and the axicon are superimposed schematically according to the topographic images. b) Cross sections of the input and output beams with Gauss and Bessel-Gaussian fits respectively. c) SNOM images of the output beam close to the sample surface (4nm) and far-away from it (100nm).

Subtracting the near-field image by the "far"-field one minimizes the contribution of the scattered field in the SNOM measurements and allows for a more quantitative analysis of the Bessel-Gaussian beam. The resulting corrected near-field image is shown on Fig. 5a. Though this manipulation leads to a strong noise close to the axicon due to the saturation of the detector (gray zone in Fig. 5a), it considerably improves the image quality of the Bessel-Gaussian beam

distribution after this. The latter image is then fitted along the propagation axis (z) by a zero-order Bessel-Gaussian function assuming that the electric field amplitude at the axicon output is:

$$E(y,z) \propto \exp(jk_z z)\, J_0\left(k_\rho, (y-y_0)\right) \exp\left(-\frac{(y-y_0)^2}{w_0^2}\right) \qquad (2)$$

where y_0 is the transverse coordinate of propagating beam and w_0=5.2µm is the waist radius of the Gaussian beam at the input. The resulting field intensity ($I=E\cdot E^*$) fitted image shown in Fig. 5b faithfully reflects the near-field measurement. The half-width w_{HF} of the central lobe of the Bessel beam is recovered from the fitted values of k_ρ along the propagation axis and it is plotted on Fig. 5c. Here we found an average beam width w_{HF} ~ 2.4µm with a depth of focus z_{max}~ 38µm. These experimental results are consistent quantitatively with the modeling predictions and thus validate the concept proposed here.

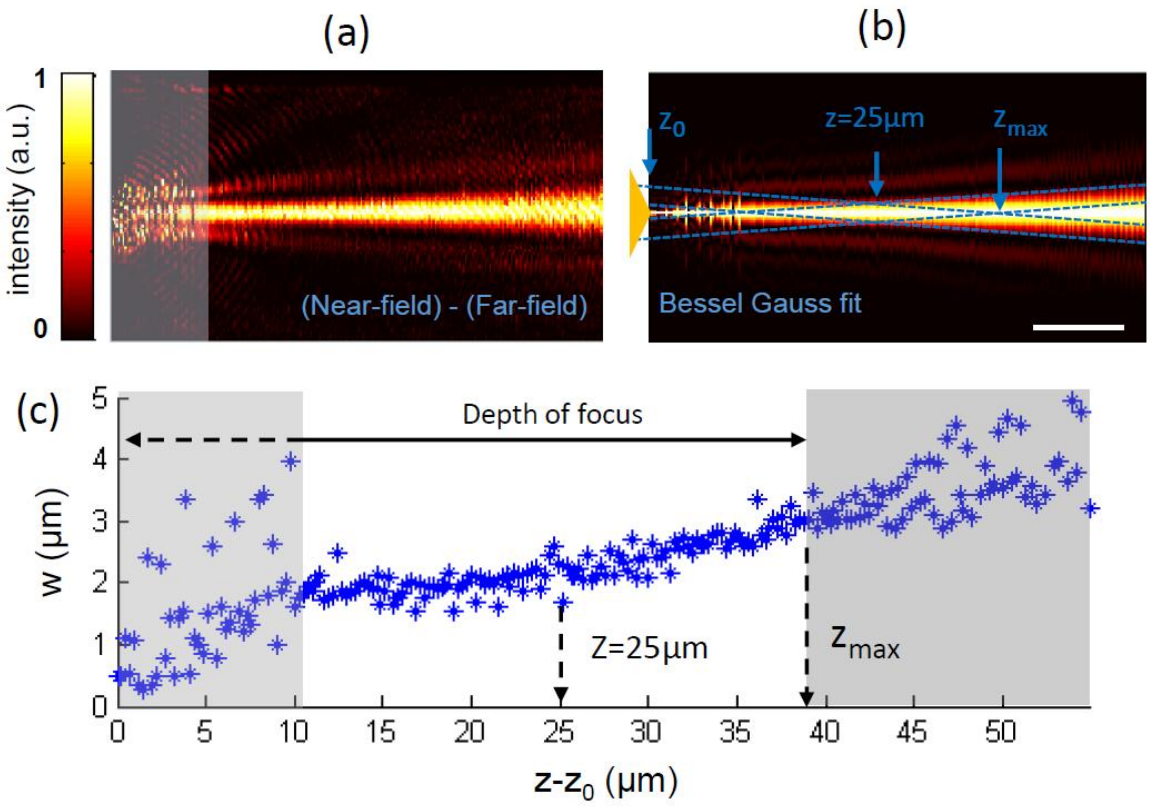

Figure 5. a) SNOM image of the output beam obtained after removing of the far-field background. Scale bar 10 μm; b) SNOM image of the output beam after the background removal. Scale bar is 10μm; c) Evolution with propagation distance of the half-width of the Bessel-Gaussian beam obtained from SNOM shown in Fig. 5b. The gray areas on the left corresponds to the zone of near-field images where the intensity is saturated just after the axicon.

In conclusion, an experimental demonstration of an integrated plasmonic axicon operating in a guided wave configuration and allowing the generation of Bessel-Gaussian intensity profile beams is reported. Near-field scanning optical microscopy technique is used to provide direct evidence of long-range propagation without diffraction of a guided beam and to determine its intensity profile. The long-distance diffraction free propagation obtained using such a metasurface-dielectric hybrid axicon lens demonstrates the ability to control the light flux in guided wave structures through local engineering of the effective index using plasmonic nanoresonators. The wide variety of physical parameters: geometrical shape, material composition, near-field interactions, can be used to control the properties of plasmonic resonators such as resonance frequency, quality factor and spectral response, enabling the design of nano-engineered optical devices with advanced performance.

Unlike photonic crystals, the current work approach based on the integration of resonant elements on top of the slab waveguide is not limited to high index materials. It is a generic technology that can be easily adapted to a wide variety of platforms, such as planar silica, silicon nitride, lithium niobate, II-VI, III-V, IV-IV semiconductors etc. The concept can also be easily adapted to other spectral domains, especially for longer wavelengths, from mid- and far infrared to THz. It can also be extended to the visible range or even to UV by considering other

plasmonic materials, such as highly doped semiconductors of high dielectric index dielectrics by exploiting the Mie resonances of nanoparticles.

METHODS

Scanning Near-field Optical Microscopy

The near-field microscope used here is a home-made SNOM system operating in collection mode with a shear-force feed-back. The SNOM system is mounted on an end-fire coupling setup in free space to inject light inside the waveguide through its cleaved facet with a proper control of the polarization. A near-field probe made of a pulled monomode fiber optics is scanned at a constant distance from the sample surface. The light collected by the probe and the shear-force signal are detected during the probe scan and optical and topographical images are obtained simultaneously.

Corresponding Author

*E-mail: anatole.lupu@c2n.upsaclay.fr

ORCID ID: 0000-0002-3060-6826

Dr. A. Lupu

Centre for Nanoscience and Nanotechnology,

CNRS, Univ. Paris-Sud, Université Paris-Saclay,

C2N – 10 Boulevard Thomas Gobert

91120 Palaiseau cedex

Phone: +3370270322

France

Author Contributions

The manuscript was written through contributions of all authors. All authors have given approval to the final version of the manuscript.

Notes

The authors declare no competing financial interest.

Acknowledgement

We would like to thank the C2N Cleanroom staff and French RENATECH network for their technological support. This work has been supported by the EIPHI Graduate School (contract "ANR-17-EUR-0002"), the FEDER Program and the Conseil Régional de Bourgogne Franche-Comté.

REFERENCES

1. Born, M.; Wolf, E. Principles of Optics-Electromagnetic Theory of Propagation, Interference and Diffraction of Light. Cambridge University Press, **1999**

2. Durnin, J. Exact solutions for nondiffracting beams. I. The scalar theory. *J. Opt. Soc. Am. A* **1987,** 4, 651–654.

3. Durnin, J.; Miceli, J. J.; Eberly, J. H. Diffraction-free beams. *Phys. Rev. Lett.* **1987,** 58, 1499–1501.

4. Bouchal, Z.; Wagner, J.; Chlup; M. Self-reconstruction of a distorted nondiffracting beam. *Opt. Commun.* **1998,** 151, 207–211.

5. Lu, J.; Greenleaf, J. F. Nondiffracting X waves exact solutions to free-space scalar wave equation and their infinite realizations. I*EEE Trans. Ultrason., Ferroelect., Freq. Control* **1992,** 39, 19-31.

6. Saari, P.; Reivelt, K. Evidence of X-shaped propagation-invariant localized light waves. *Phys. Rev. Lett.* **1997,** 79, 4135-4138.

7. Alexeev, I.; Kim, K. Y.; Milchberg, H. M. Measurement of the Superluminal Group Velocity of an Ultrashort Bessel Beam Pulse. *Phys. Rev. Lett.* **2002,** 88, 073901.

8. Bowlan, P.; Valtna-Lukner, H.; Lõhmus, M.; Piksarv, P.; Saari, P.; Trebino, R. Measuring the spatiotemporal field of ultrashort Bessel-X pulses. *Opt. Lett.* **2009,** 34, 2276-2278.

9. Chen, J.; Ng, J.; Lin, Z. F.; Chan, C. T. Optical pulling force. *Nat. Photon.* **2011,** 5, 531–534.

10. Dogariu, A.; Sukhov, S.; Jose Sáenz, J. Optically induced 'negative forces'. *Nat. Photon.* **2013,** 7, 24–27.

11. Hafizi, B.; Esarey, E.; Sprangle, P. Laser-driven acceleration with Bessel beams. *Phys. Rev. E* **1997,** 55, 3539–3545.

12. Arlt, J.; Dholakia, K. Generation of high-order Bessel beams by use of an axicon. *Opt. Commun.* **2000,** 177, 297–301.

13. Arlt, J.; Dholakia, K.; Soneson, J.; Wright. E. Optical dipole traps and atomic waveguides based on Bessel light beams. *Phys. Rev. A* **2001,** 63, 1–8.

14. Schmid, S.; Thalhammer, G.; Winkler, K.; Lang, F.; Denschlag, J. H. Long distance transport of ultracold atoms using a 1D optical lattice. *New J. Phys.* **2006,** 8, 159.

15. Arlt, J.; Garces-Chavez, V.; Sibbett, W.; Dholakia, K. Optical micromanipulation using a Bessel light beam. *Opt. Commun*. **2001,** 197, 239–245.

16. Garcés-Chávez, V.; McGloin, D.; Melville, H.; Sibbett, W.; Dholakia, K. Simultaneous micromanipulation in multiple planes using a self-reconstructing light beam. *Nature* **2002,** 419, 145–147.

17. Wulle, T.; Herminghaus, S. Nonlinear optics of Bessel beams. *Phys. Rev. Lett.* **1993,** 70, 1401–1404.

18. Peet, V.; Tsubin, R. Third-harmonic generation and multiphoton ionization in Bessel beams. *Phys. Rev. A* **1997,** 56, 1613–1620.

19. Klewitz, S.; Sogomonian, S.; Woerner, M.; Herminghaus, S. Stimulated Raman scattering of femtosecond Bessel pulses. *Opt. Commun.* **1998,** 154, 186–190.

20. Planchon, T. A.; Gao, L.; Milkie, D. E.; Davidson, M. W.; Galbraith, J. A.; Galbraith, C. G.; Betzig, E. Rapid three-dimensional isotropic imaging of living cells using Bessel beam plane illumination. *Nat. Methods* **2011,** 8, 417–423.

21. Meyers, R. E.; Deacon, K. S.; Tunick, A. D.; Shih, Y. Virtual ghost imaging through turbulence and obscurants using Bessel beam illumination. *Appl. Phys. Lett.* **2012** 100, 061126.

22. Erdelyi, M.; Horvath, Z.; Szabo, G.; Bor, Z.; Tittel, F.; Cavallaro, J.; Smayling, M. Generation of diffraction-free beams for application in optical microlithography. *J. Vac. Sci. Technol. B* **1997,** 15, 287–292.

23. Yalizay, B.; Ersoy, T.; Soylu, B.; Akturk, S. Fabrication of nanometer-size structures in metal thin films using femtosecond laser Bessel beams. *Appl. Phys. Lett.* **2012,** 100, 031104.

24. Lemaitre-Auger, P.; Abielmona, S.; Caloz, C. Generation of Bessel Beams by Two-Dimensional Antenna Arrays Using Sub-Sampled Distributions. *IEEE Trans. Antennas Propag.* **2013,** 61, 1838–1849.

25. Tiwari, S. K.; Mishra, S. R.; Ram, S. P.; Rawat, H. S. Generation of a Bessel Beam of Variable Spot Size. *Appl. Opt.* **2012,** 51, 3718-3725.

26. Herman, R. M.; Wiggins, T. A. Production and uses of diffractionless beams. *J. Opt. Soc. Am. A* **1991,** 8, 932.

27. Yu, N.; Capasso, F. Flat optics with designer metasurfaces. *Nature materials* **2014,** 13, 139.

28. Kildishev, A. V.; Boltasseva, A.; Shalaev, V. M. Planar photonics with metasurfaces. *Science* **2013,** 339, 1232009.

29. Aieta, F.; Genevet, P.; Kats, M. A.; Yu, N.; Blanchard, R.; Gaburro, Z.; Capasso, F. Aberration-Free Ultrathin Flat Lenses and Axicons at Telecom Wavelengths Based on Plasmonic Metasurfaces. *Nano Lett.* **2012,** 12, 4932−4936.

30. Khorasaninejad, M.; Aieta, F.; Kanhaiya, P.; Kats, M. A.; Genevet, P.; Rousso, D.; Capasso, F. Achromatic metasurface lens at telecommunication wavelengths. *Nano Lett.* **2015,** 15, 5358-5362.

31. Chen, W. T.; Khorasaninejad, M.; Zhu, A. Y.; Oh, J.; Devlin, R. C.; Zaidi, A.; Capasso, F. Generation of wavelength-independent subwavelength Bessel beams using metasurfaces. *Light Sci. Appl.* **2017,** 6, e16259.

32. Li, Y. B.; Cai, B. G.; Wan, X.; Cui, T. J. Diffraction-free surface waves by metasurfaces. *Opt. Lett.* **2014** 39, 5888–5891.

33. Qi, M. Q.; Tang, W. X.; Cui, T. J. A broadband Bessel beam launcher using metamaterial lens. *Sci. Rep.* **2015,** 5, 11732.

34. Marciante, J. R.; and Agrawal, G. P. Spatio-temporal characteristics of filamentation in broad-area semiconductor lasers. IEEE Journal of Quantum Electronics **1997**, 33 1174-1179.

35. Zhu L.; Chak P.; Poon J. K. S.; DeRose G. A.; Yariv A.; and Scherer A. Electrically-pumped, broad-area, single-mode photonic crystal lasers. *Opt. Express* **2007**, 15 5966-5975.

36. Zengerle, R. Light-Propagation in Singly and Doubly Periodic Planar Wave- Guides. J. Mod. Opt. 1987, 34, 1589-1617.

37. Kosaka, H., Kawashima, T., Tomita, A., Notomi, M., Tamamura, T., Sato, T., & Kawakami, S. Self-collimating phenomena in photonic crystals. Appl. Phys. Lett. 1999, 74, 1212-1214.

38. Dellinger, J., Bernier, D., Cluzel, B., Le Roux, X., Lupu, A., de Fornel, F., & Cassan, E. Near-field observation of beam steering in a photonic crystal superprism. Opt. Lett. 2011, 36, 1074-1076.

39. Lupu, A.; Dubrovina, N.; Ghasemi, R.; Degiron, A.; De Lustrac, A. Metal-Dielectric Metamaterials for Guided Wave Silicon Photonics. *Opt. Express* **2011,** 19, 24746−24761.

40. Fan, Y.; Le Roux, X.; Lupu, A.; and de Lustrac, A. Ultra-compact on-chip metaline-based 1.3/1.6 μm wavelength demultiplexer. *Photonics Research* **2019** 7, 359-362.

41. Fan, Y.; Le Roux, X.; Korovin, A.; Lupu, A.; De Lustrac, A. Integrated 2D-Graded Index Plasmonic Lens on a Silicon Waveguide for Operation in the Near Infrared Domain. *ACS Nano* **2017**, 11, 4599−4605.

42. Andryieuski, A.; Malureanu, R.; Lavrinenko, A.V. Wave propagation retrieval method for metamaterials: Unambiguous restoration of effective parameters. *Phys. Rev. B* **2009**, 80, 193101.

43. Andryieuski, A.; Ha, S.; Sukhorukov, A.A.; Kivshar, Y.S.; Lavrinenko, A.V. Bloch-mode analysis for retrieving effective parameters of metamaterials. *Phys. Rev. B* **2012**, 86, 035127.

44. Palik, E.D. *Handbook of Optical Constants of Solids.* Academic Press, **1998**.

45. https://www.ansys.com/fr-fr/products/electronics/ansys-hfss (last access 2019-05-03)